FRAGMENTS DISTRIBUTION PREDICTION FOR ENVISAT CATASTROPHIC FRAGMENTATION

Lorenzo Olivieri[(1)], Cinzia Giacomuzzo[(2)], Cristina Duran-Jimenez[(3)] , Alessandro Francesconi[(4)], Camilla Colombo[(5)]

[(1)] CISAS "G. Colombo", University of Padova, Via Venezia 15, 35131 Padova (PD), Italy, Email: lorenzo.olivieri@unipd.it
[(2)] DII, University of Padova, Via Venezia 1, 35131 Padova (PD), Italy, Email: cinzia.giacomuzzo@unipd.it
[(3)] Politecnico di Milano, Milano (MI), Italy, Email: cristina.duran@mail.polimi.it
[(4)] DII / CISAS "G. Colombo", University of Padova, Via Venezia 1, 35131 Padova (PD), Italy, Email: alessandro.francesconi@unipd.it
[(5)] DAER, Politecnico di Milano, Milano (MI), Italy, Email: camilla.colombo@polimi.it

ABSTRACT

ENVISAT is currently one of the largest debris in Low Earth Orbit and it resides in a highly populated orbital zone with higher impact risk. A collision with other satellites or rocket stages could generate and scatter fragments into altitudes occupied by many operational spacecraft, and in the worst case could restrict the access to polar orbits at about 800 km altitude. In this context, there is a need to evaluate the contamination of the orbital regions possibly involved by the spread of debris originated after a possible ENVISAT fragmentation.

In this paper the results of a campaign of hypervelocity impacts simulations with ENVISAT as target body are presented. A set of potential configurations for the collision have been simulated, varying the impacting body (small-class 100 kg satellite, defunct rocket stage) as well as the impact position (glancing impact on ENVISAT radiator, collision on the central body); for each impact configuration, fragments distributions are reported and the severity of different collision scenarios is discussed. Then, newly generated fragments are propagated to identify and assess local variations of the space debris spatial density. This is achieved by overlaying ENVISAT fragments population to ESA Meteoroid and Space Debris Terrestrial Environment Reference (MASTER) population and studying their evolution with a continuum model.

1 INTRODUCTION

The risk of polluting the space environment with artificial debris has been recognised since the beginning of the space era [1]. In the last decade, further concern has arisen due to the small satellites market growth [2][3] and the commercial plans for large constellations [4][5][6][7], that would further impact the sustainability of the near-Earth orbits [8][9][10]. In fact, as the number of spacecraft in Earth orbit increases, the probability of collisions between them also increases [11]. In case of collision events, such as the Cosmos-Iridium one [12], the generated fragments are not limited to the involved altitudes but can contaminate neighbourhood orbits. In this context, the scientific community has been investigating the current resident objects population to identify the worst potential offenders, whose fragmentation might cause catastrophic contamination of near-Earth orbits [13][14][15]; these studies indicate the relict of ENVISAT among the most dangerous ones. This large spacecraft (about 7 ton [16][17]) was lost in 2012, probably due to a small debris impact, turning the Earth-observation satellite in an uncontrolled body, slowly tumbling at an altitude of 800 km [18][19], with an expected natural decay time of more than 150 years. In addition, ENVISAT orbit is already crowded with both controlled and uncontrolled objects: before the unexpected mission termination, the spacecraft performed few collisions avoidance manoeuvres [20], that the defunct satellite cannot perform anymore. For these reasons, ENVISAT ranks among the first positions for future Active Debris Removal missions [21][22][23].

Consequently, there is a need to evaluate the contamination of the orbital regions affected by the spread of debris originated after a possible ENVISAT fragmentation. To date, no detailed model of the spacecraft fragmentation is available in literature, as any fragments distribution is strongly influenced by the collision scenario. Without these models, the propagation of the fragments population generated by a potential collision with ENVISAT cannot be performed. In this context, this paper aims to investigate different collision scenarios, varying the impacting body as well as the impact position, and to propagate the newly generated fragments to identify and assess local variations of the space debris density.

1.1 Models and tools for spacecraft fragmentation

Currently, empirical and semi-empirical breakup models are the most common means to provide detailed descriptions of fragments clouds originated by catastrophic collisions. The NASA Standard Breakup Model (SBM, [24]) provides an empirical tool to calculate fragments mass, velocity, area-to-mass, and characteristic length distributions. The SBM is based on empirical data, including a series of ground-based tests called SOCIT ([25][26][27]); updates are expected in the next few years thanks to the inclusion of new laboratory test [28]. Among the limitations of this tool, NASA SBM does not consider the low-velocity regime, and refers only to "bulky" spacecraft hit on the centre of mass, with full transfer of the impactor energy to the target. To partially address these limitation, the semi-empirical tools, FAST ([29][30]) and IMPACT ([31][32]) provide simple and fast-running models based on mass, momentum, and energy conservation.

Other simulations approaches, e.g. based on the use of finite elements, discrete elements, hydrocodes, or combinations of these techniques, are still in infancy because of the complexity of the physical problem, the large scales involved, and, most critical, the massive computational effort requested to analyse collisions with large multipart objects such as entire satellites.

In this context, a new tool, called Collision Simulation Tool Solver (CSTS), was developed in the framework of the ESA contract "Numerical simulations for spacecraft catastrophic disruption analysis". The key features of CSTS are the capability of modelling a large variety of collision scenarios involving complex systems such as entire satellites and the possibility to provide statistically accurate results with a computational effort orders of magnitude lower than hydrocodes [33]. The underlying idea of the CSTS is to model the colliding objects with a coarse mesh of Macroscopic Elements representing major satellite parts connected by structural links to form a system-level net. Macroscopic Elements represent spacecraft elementary building blocks, such as plates, sandwich panels, joints, etc. The CSTS was successfully subjected to a first validation campaign involving both simple targets (plates, Whipple Shields) and sub-scale satellite models [33], demonstrating the capability of well reproducing the experiments outcomes. In addition, the tool was employed in parametric studies to evaluate the transition from low to hypervelocity impacts [34] and the effect of structural integrity on fragmentation processes [35]. In this paper, fragmentation simulations are executed with the CSTS; a selection of the results is presented accordingly to simulations elaboration state.

Results in terms of generated debris distributions are used as input to describe the evolution of the fragmentation cloud in the orbital environment. A continuum methodology proposed in [36], is here employed to investigate the time evolution of the debris band.

1.2 Paper contents

This paper is organised as follows. Section 2 present the spacecraft models implemented in the CSTS simulations and Section 3 describes the investigated collision scenarios. Section 4 presents simulations results and compare the generated fragments distributions with the NASA SBM. In Section 5, the fragmentation cloud propagation model is introduced; the application to one collision scenario is presented in Section 6 to identify and assess local variations of the total space debris density.

2 SPACECRAFT COLLISION SIMULATIONS

The collision scenarios selected for this paper intend to explore the effect of impact velocity, impact point, and impacting body on ENVISAT fragmentation. It is currently assumed that catastrophic impacts (i.e. causing the total fragmentation of the impacted body) occur when the kinetic energy of the impactor is higher than 40 Joule per unit mass of the target (energy-to-mass ratio EMR>40 J/g). The selected configurations include impacts whose EMRs are both below and over this threshold. In addition, models such as the NASA SBM do not contemplate potential dissipation effects in glancing impacts; considering that the Iridium-Cosmos event has been speculated to be a glancing impact, it is worth to investigate collisions both on ENVISAT centre of mass and appendages. Two different impactors are selected, a small-class 100 kg satellite based on JAXA SDS-1 [37], and a rocket stage based on the 4-ton second stage of the Long March CZ2C [38].

2.1 ENVISAT model

A custom-made geometric model of ENVISAT is employed as target in the CSTS simulations. The model features the same elements of the real spacecraft, with structural components, the solar array, and the scientific instrumentation [16][17]. The spacecraft geometric model in CST is shown in Fig. 1. It contains 223 Macroscopic Elements, reproducing the subsystems and the systems specified in Tab. 1 [17]. The baseline choice for elements' material is aluminium alloy, since it features a ductile structural behaviour, while solar panels are CFRP to simulate a brittle fracture. In some cases, where subsystems incorporating multiple materials and/or multiple components are concerned (propellant tanks, batteries, electronic boxes), the density is reduced to the elements "equivalent density" that matches the real mass of the component. The links connecting Macroscopic Elements are modelled to

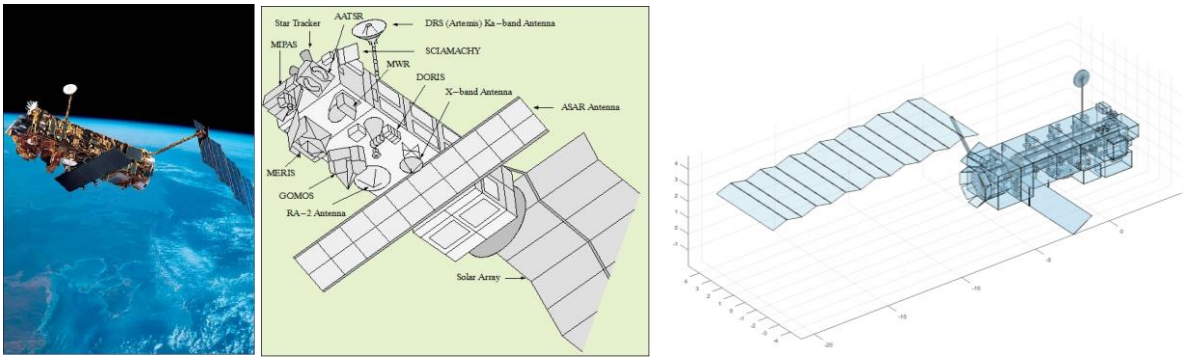

Figure 1: ENVISAT artistic representation (left), main elements (centre)[17] and CSTS model (right)

Table 1: ENVISAT geometric model characteristics and elements (data from [17])

Mass	> 8000 kg	
Main body size	1.6 x 2.750 x 1.6 m	
Service module size	2.360 x 2.750 x 2.075 m	
Solar array size	1.0 x 4.970 x 0.00175 m	
Main components	XBAND ANTENNA	
	STAR TRACKER	
	PAYLOAD MODULE CENTRAL TUBE	
	TANKS	
	BATTERIES	
	ELETTRONICS	
Instrumentation	ASAR	DORIS
	RA	MERIS
	DRS	MIPAS
	MWR	AATSR
	GOMOS	SCIAMACHY

Table 2: List of the simulated impact scenarios

Simulation ID	Impactor	Impact velocity, km/s	Impact point	EMR, kJ/kg
E-1	Small Satellite	1	Central body	0.78
E-2	Small Satellite	1	Appendage	
E-3	Small Satellite	10	Central body	78.1
E-4	Small Satellite	10	Appendage	
E-5	Rocket stage	1	Central body	31.3
E-6	Rocket stage	1	Appendage	
E-7	Rocket stage	10	Central body	3125.0
E-8	Rocket stage	10	Appendage	

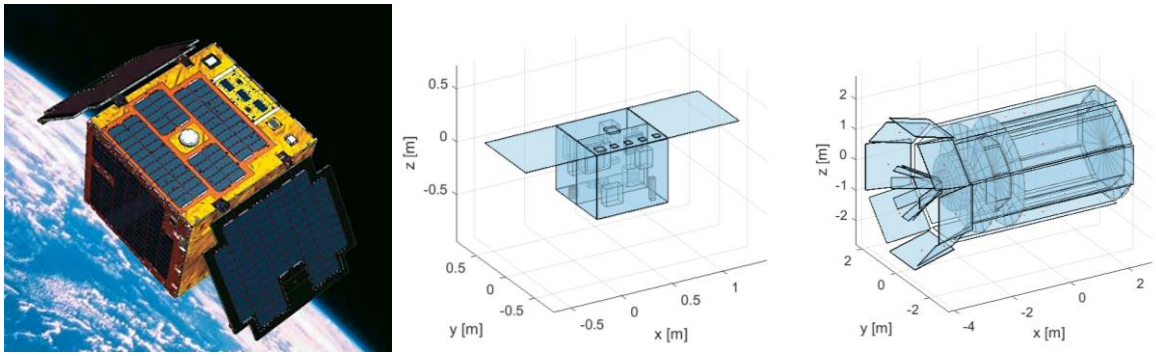

Figure 2: JAXA SDS-1 artistic representation (left, [37]) and CSTS geometric model (centre); Long March CZ2C second stage CSTS geometric model (right).

represent the mechanical connections between the real S/C components.

2.2 Impactors models

The small satellite is based on the 100 kg JAXA SDS-1 spacecraft [37] and can be seen in Fig. 2. Its size is 70cm×70cm×60cm. Design details are available online for this spacecraft, that was already modelled for validation simulations in CSTS. The geometric model can be seen in Fig. 2 (centre) and consists of 35 linked macroscopic elements; the selected materials are again aluminium and CFRP.

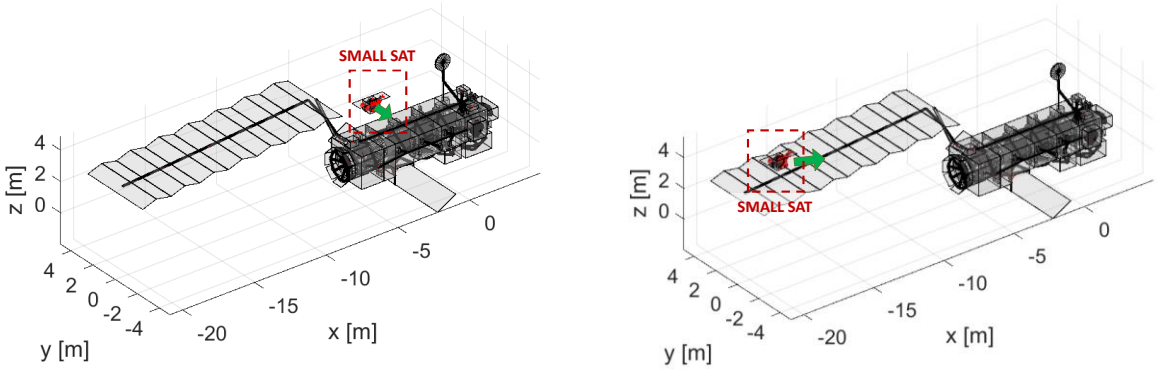

Figure 3: Small sat impacts on ENVISAT centre of mass (configurations E1 and E3, left) and appendage (configurations E2 and E4, right)

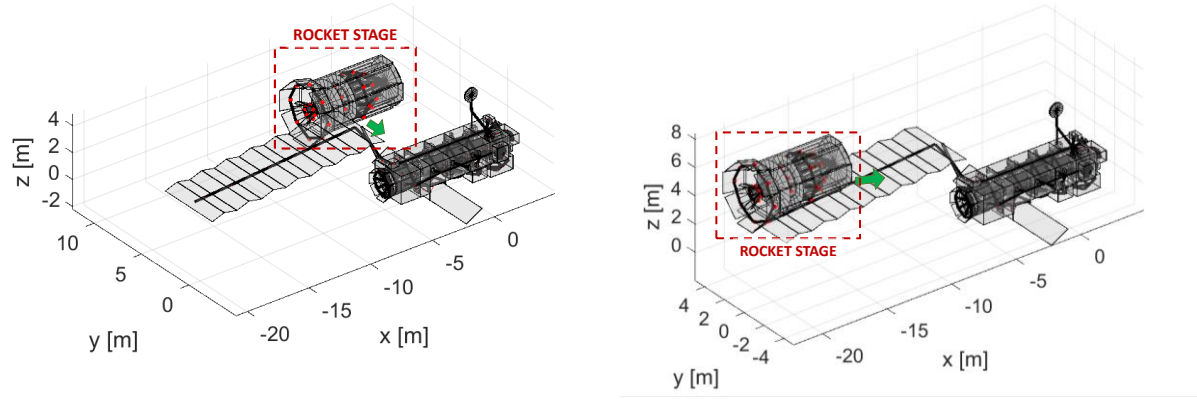

Figure 4: Rocket stage impacts on ENVISAT centre of mass (configurations E5 and E7, left) and appendage (configurations E6 and E8, right)

The rocket stage model (Fig. 2, right) is based on the 4-ton second stage of the Long March CZ2C. The geometric model consists in 49 aluminium linked Macroscopic Elements. Complex features such as the nozzle are simplified with a series of radial plates. In some cases, where subsystems incorporating multiple materials and/or multiple components are concerned, an equivalent thickness is considered for the elements to match the real mass of the component.

3 COLLISION SCENARIOS

Eight collision scenarios are examined; in addition to two different impactors (small satellite and rocket stage) and two impact points (ENVISAT centre of mass and appendage), two impact velocities are considered (1 and 10 km/s). Tab. 2 shows the eight simulated configurations, reporting for each case the impact EMR; it shall be noted that the EMR calculation is not affected by the impact point. The 1 km/s collisions envisage an EMR below the 40 kJ/kg classic catastrophic threshold; in particular, the configuration with the small satellite as impactor is well below such threshold, while the rocket stage scenario provides an intermediate situation with an EMR of about 31 kJ/kg. For the second velocity, the EMR is always over the catastrophic threshold.

The simulated scenarios are shown in Fig. 3 and Fig. 4. According to the NASA SBM, the two impact points (ENVISAT centre of mass and appendage) lead to the same result in terms of objects' fragmentation for a given EMR, since the total mass of the event is the same in both situations. However, the involvement of appendages may contribute to dampen the impact energy, and hence different impact consequences are expected in the two cases.

4 SIMULATION RESULTS AND DISCUSSION

For each of the collision scenarios described in Section 2, simulation results are reported in the form of cumulative characteristic length distributions of fragments larger than 1 cm, as obtained with CSTS and NASA SBM. As stated before, for the low-velocity impacts, the EMR is always under the catastrophic fragmentation threshold of 40 kJ/kg; in this case the comparison with the NASA SBM subcatastrophic model is also reported.

Among the considered scenario, only simulations E-1,

E-2, E-5, and E-7 have reached conclusion (i.e. depletion of the fragmentation processes). Results for the other simulations are partial but still give important indications on ENVISAT fragments distributions. Characteristic length distributions can be seen in Fig. 5 (small satellite impactor) and Fig. 6 (rocket stage impactor). In general, it is shown that:

- In all cases, the number of fragments is increased with impact velocity rising from 1 to 10 km/s;
- In all the completed simulations, the fragments distributions are well below the NASA SBM prediction; for the impacts at 1 km/s, the curves are also well below the subcatastrophic prediction.
- In most simulation cases, ENVISAT is not completely disintegrated: several large pieces with $L_c > 1$ m remain intact.

Concerning the small satellite impact at the lower velocity, the EMR of simulations E-1 and E-2 is 0.78 kJ/kg, well below the catastrophic threshold. Fig. 5 (left), shows negligible variations in L_c distributions for impacts at the centre of mass (solid red line) and on

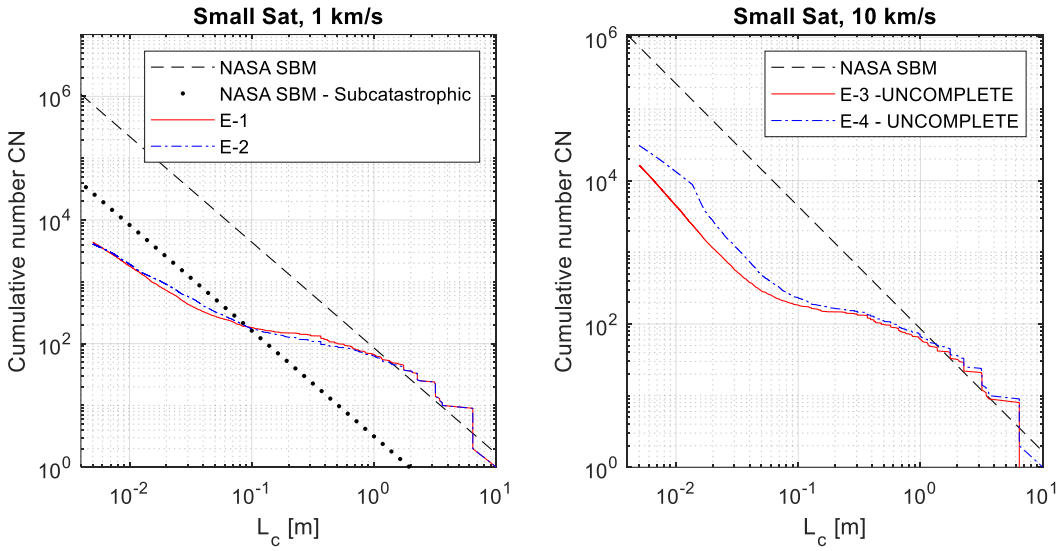

Figure 5: L_C distribution curves for the small satellite impact on ENVISAS at 1 km/s (left, compared to NASA SBM, dashed black line, and NASA SBM subcatastrophic, dotted black line) and at 10 km/s (right, compared to NASA SBM, dashed black line). Impact on ENVISAT centre of mass is reported with the red solid line, impact on the appendage with the blue dashed-dotted line.

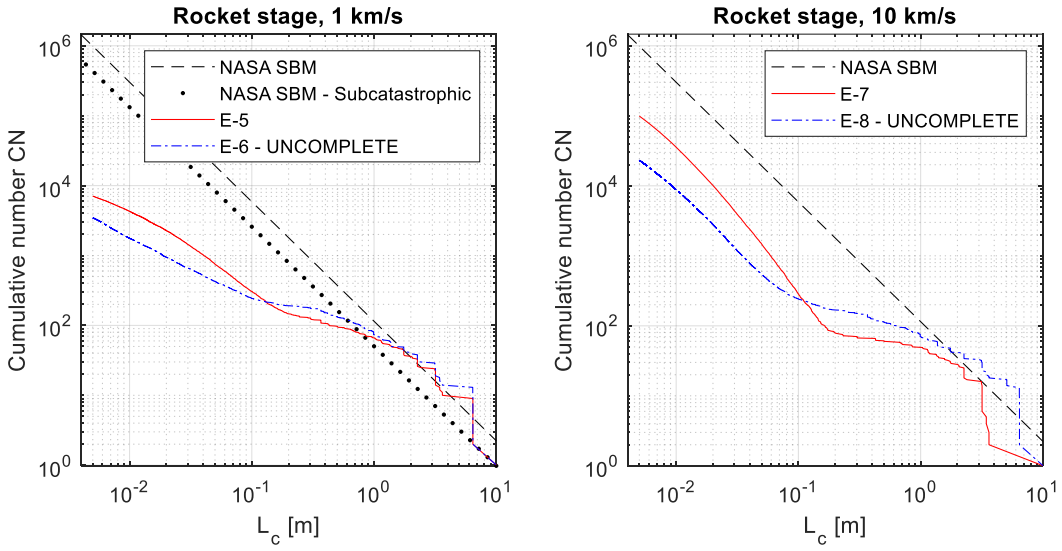

Figure 6: L_C distribution curves for the second stage impact on ENVISAS at 1 km/s (left, compared to NASA SBM, dashed black line, and NASA SBM subcatastrophic, dotted black line) and at 10 km/s (right, compared to NASA SBM, dashed black line). Impact on ENVISAT centre of mass is reported with the red solid line, impact on the appendage with the blue dashed-dotted line.

ENVISAT appendage (dashed-dotted blue line). In both cases the curve is above the subcatastrophic NASA SMB for L_c > 10 cm and below it for smaller characteristic lengths. This can be related to the relatively small impact energy, that causes the dissolution of the internal links between ENVISAT Macroscopic Elements but cannot trigger the complete fragmentation of most of them. In addition, the slight difference in the ranges 1-10 cm (more fragments for the impact on the appendage) and 10-100 cm (less fragments for the impact on the appendage) can be related to the fragmentation of ENVISAT solar array, that in case of appendage impact (E-2) is directly hit by the colliding small satellite, while in the centre of mass impact (E-1) is only marginally involved in the collision.

Fragments characteristic length distribution from scenario E-3 and E-4 (small satellite at 10 km/s, EMR of 78.1 kJ/kg) can be seen in Fig. 5 (right). Both simulations, the collision on ENVISAT centre of mass, (solid red line) and the collision on appendage (dash-dot blue line) are still running. The following results can be noted:

- Both curves are well below the NASA SBM prediction for fragments with L_c < 1 m.
- Although preliminary, the characteristic length distribution for scenario E-4 (impact on appendage) shows a finer fragmentation for L_c < 20 cm. It is expected that the prosecution of this simulation will further shatter the existing fragments, drawing the characteristic length distribution closer to the NASA SBM prediction.

It can be concluded that for the small satellite impactor (mass of 100 kg, ~1/80 of ENVISAT) the appendage does not act as shield for the spacecraft.

For the collision scenarios considering the rocket stage (Fig. 6), simulations duration is affected by the complexity and the mass (about 1/2 of ENVISAT) of the impacting body: only simulations E-5 and E-7 have reached conclusion. In any case, the following observations can be discussed:

- the number of fragments still increases with impact velocity rising from 1 (left) to 10 km/s (right).
- The fragments distributions for the two scenarios with impacts on the central body (E-5 and E-7) are well above the equivalent simulations with the small satellite (E-1 and E-3).
- For the low velocity case (left) the completed simulation is well below the NASA SBN prediction.
- For completeness, Fig. 6 (left) include the subcatastrophic NASA SBM prediction curve. This model assumes a large target that is cratered by a much smaller projectile; by contrast, the impact configuration (EMR 31.3 kJ/kg, near the catastrophic threshold) and the impactor mass (about 1/2 of ENVISAT) suggest that this model is not representative of the two scenarios.
- Simulation E-7 (10 km/s, impact on ENVISAT centre of mass) is about one order of magnitude below the NASA SBM prediction.
- The effect of the appendage in the fragmentation process cannot be addressed with the current uncompleted results.

In general, results suggest that the NASA SBM over-estimates the fragmentation process for all the selected cases.

4.1 Area to mass ratio

Figs. 7 to 9 compare area to mass ratio distributions for some of the investigated scenarios. The effect of the impactor mass can be seen in Fig. 7: both the small satellite (simulation E-1, yellow) and the rocket stage (E-5, light blue) collide with ENVISAT at 1 km/s on its centre of mass. It can be observed that the cumulative number of fragments is higher for the rocket stage, as the distribution bell is larger. In addition, the distribution peak is not centred at the same value of the A/m ratio, because (1) the two impactors have a slightly different material composition, and (2) the ENVISAT elements involved in the fragmentation process are different due to the different sizes of the impactors.

The area to mass ratio distributions for the rocket stage impact on the centre of mass at 1 km/s (light blue) and 10 km/s (pink) are compared in Fig. 8. While the shape and the position of the peak are comparable, the effect of the velocity can be clearly observed in the different number of generated fragments.

Fig. 9 compares the A/m ratio distribution for the two impact points (ENVISAT centre of mass, yellow, and appendage, red) for the small satellite collision at 1 km/s. It can be observed that the distribution peak for the E-1 scenario is more prominent, while the appendage impact (E-2) shows a slightly higher number of fragments in the range between -1 and -0.5 m^2/kg. This difference is clearly correlated to the presence of the solar panel fragments in scenario E-2, whose A/m ratio is higher than the one from Macroscopic Elements from ENVISAT main body. Comparing the characteristic length curves in Fig. 5 to the A/m ratio in Fig. 9, it can be observed that similar L_c distributions do not imply comparable A/m ratio ones.

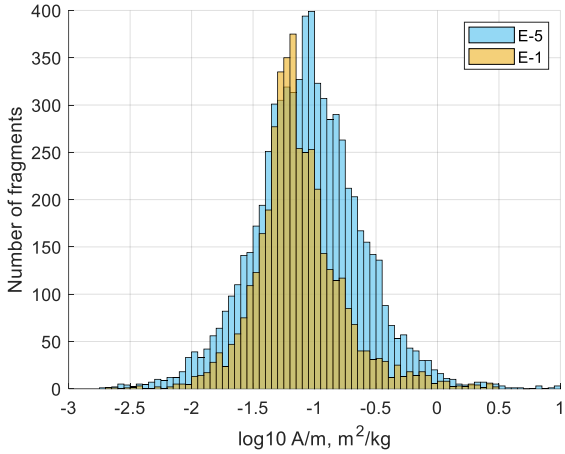

Figure 7: Area to mass ratio distributions comparison for scenarios E-5 (light blue) and E-1 (yellow)

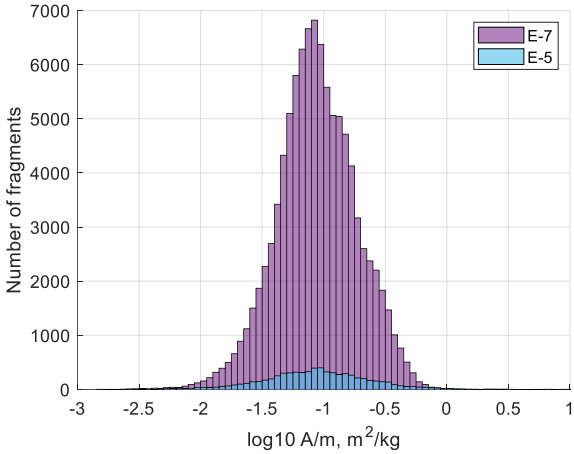

Figure 8: Area to mass ratio distributions comparison for scenarios E-7 (pink) and E-5 (light blue)

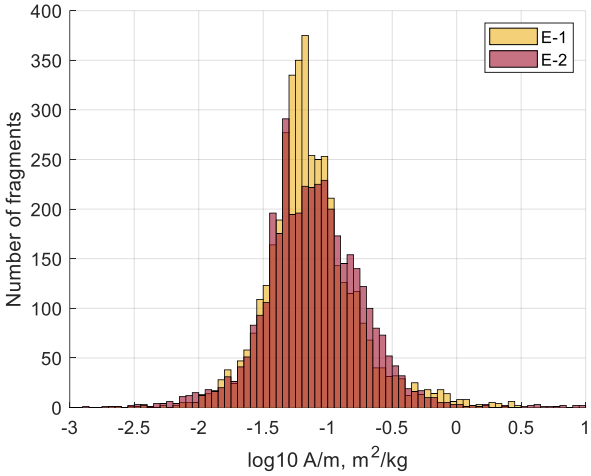

Figure 9: Area to mass ratio distributions comparison for scenarios E-1 (yellow) and E-2 (red)

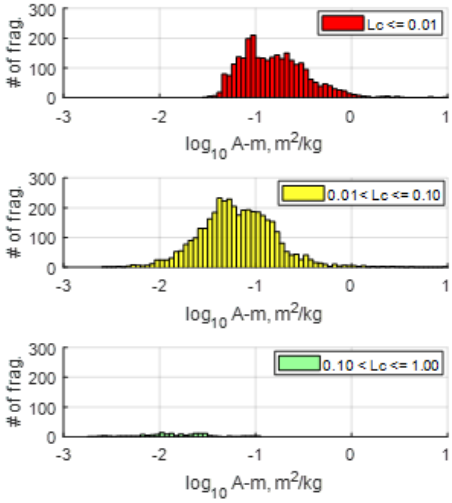

Figure 10: Area to mass ratio distributions at different characteristic length ranges for scenario E-5

Finally, Fig. 10 shows that area to mass distributions may vary depending on different characteristic length classes. The distributions are related to scenario E-5 (rocket stage, 1 km/s impact on centre of mass): for larger fragments, the distribution peak is at about 0.01 m^2/kg, that increases at 0.04 m^2/kg for fragments in the range 0.01-0.1 m and at 0.1 m^2/kg for the smaller fragments (Lc<0.01 m).

5 PROPAGATION OF THE FRAGMENTATION CLOUD

Based on the work in [40], an efficient method is developed, to describe the evolution in time of the fragmentation cloud. The algorithm implementing this method is structured according to the following blocks (see Fig. 11):

- The CSTS ENVISAT breakup model, that characterises the fragments generated from the collision, in terms of characteristic length, area to mass ratio and velocity.
- A numerical long-term propagator to determine the evolution in time of the orbital elements of the produced fragments, until the continuum formulation in [46] becomes applicable.
- The spatial density function, defined to translate the orbital parameters of each single fragment into a continuous function depending only on the altitude.
- A numerical propagator to describe the evolution in time of the spatial density function, from the band formation instant onward.

5.1 Band formation and numerical propagation

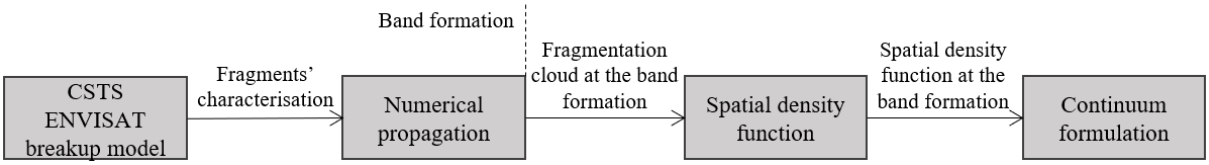

Figure 11: Schematics of the algorithm for the propagation of the fragmentation cloud

5.1.1 Band formation

The dispersion model of a fragmentation cloud can be divided into three phases, according to [41]. In the first phase, right after the collision, the produced fragments form an ellipsoid-shaped cloud concentrated at the location where the fragmentation event took place. The Earth's oblateness causes a variation on the argument of perigee ω, so the initial cloud is spread out along the parent orbit, forming a toroid (phase two). The change on the right ascension of the ascending node Ω, again, due to the Earth's oblateness, gradually dismantles the toroid. In the final configuration (phase three), the cloud forms a band around the Earth, limited in latitude by the inclination of the parent orbit. During this phase, atmospheric drag can be considered to be the dominant perturbation [41], since ω, Ω and the true anomaly θ are randomised. Consequently, the continuum formulation in [46], which takes into account only the atmospheric drag effect, can be applied only after the band formation, while a numerical propagator is needed to follow the first phases of the cloud evolution.

Adopting the approach presented in [40], the band formation time is estimated as $T_B = 3\,T_b$, where T_b is the expression for the band formation time proposed by Ashenberg [42]. T_b is defined as the maximum between the time of dispersion of the argument of perigee, T_ω, and the time of dispersion of the right ascension of the ascending node, T_Ω.

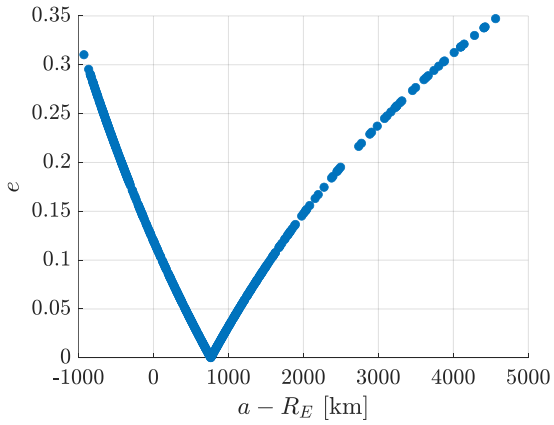

Figure 12: Semimajor axis, a, and eccentricity, e, distribution, for scenario E-5. In the figure, R_E denotes the radius of the Earth

5.1.2 Numerical propagation

Once the fragments are generated and characterised, their associated position and velocity vectors are computed. Then, the Keplerian elements defining each fragment orbit right after the collision are obtained. As reference, in Fig. 12, the Gabbard diagram characterising the initial fragmentation cloud is reported, for scenario E-5.

The evolution in time of the fragments' Keplerian elements is computed from the numerical integration of Gauss' planetary equations [43], considering atmospheric drag and Earth's oblateness perturbations. Drag effect is estimated assuming an exponential density model:

$$\rho = \rho_{ref} \exp\left(-\frac{h - h_{ref}}{H}\right) \tag{3}$$

where ρ is the atmosphere density, h is the altitude and h_{ref} is the reference altitude where the reference density ρ_{ref} and the scale height H are defined. The reference values are taken from [43]. The reference altitude h_{ref} is selected as the closest tabulated value to the altitude where the fragmentation event takes place and its value is kept constant for the entire simulation; drag effect is considered up to a 1000 km altitude and atmosphere rotation is not taken into account.

The effect of atmospheric drag is computed through the expressions reported in [44], describing the secular variation of the orbital elements. Regarding the Earth's oblateness perturbation, only the long-term effect of J_2 is considered. This assumption is made since, over the long-term, the Earth's oblateness only affects ω and Ω and, consequently, high-precision modelling of this perturbation is not essential.

The numerical integration process is halted if the fragment perigee altitude falls below 50 km, since, under this condition, the fragment is considered to be re-entering through the atmosphere [40].

5.2 Spatial density function

Once the band is formed, the information on each single fragment is translated into a total continuous density function.

Here, the spatial density function is built on the probability of finding a fragment at a distance r from

the centre of the Earth, given the semimajor axis a and the eccentricity e of its orbit. Taking the expression reported in [45], the spatial density function $n_i(r)$ defining the contribution of fragment i is

$$n_i(r) = \frac{1}{4\pi^2 r a_i \sqrt{(r - r_{p_i})(r_{a_i} - r)}} \quad (4)$$

where r_{p_i} and r_{a_i} are, respectively, the periapsis and the apoapsis of the fragment's orbit:

$$r_{p_i} = a_i(1 - e_i) \quad r_{a_i} = a_i(1 + e_i) \quad (5)$$

In order to build the total spatial density function, the contribution of each fragment in the fragmentation cloud must be considered

$$n(r) = \sum_{i=1}^{N} n_i(r) \quad (6)$$

where N is the total number of objects constituting the fragmentation cloud at the band formation.

5.3 Continuum propagation

Once the spatial density function is built at the band formation instant, the continuity equation is used to compute the density function evolution in time, under the effect of atmospheric drag. Here, the approach developed by McInnes [45] is followed. However, instead of using an analytical expression for the density function propagation, the differential equations are numerically integrated.

Assuming that no discontinuous events occur (sources, like launches; or sinks, as active debris removal), the continuity equation can be written as

$$\frac{\partial n}{\partial t} + \nabla \cdot \mathbf{f} = 0 \quad (7)$$

where n is the density function, t is the time and the term $\nabla \cdot \mathbf{f}$ models the involved continuous phenomena, in this case, the atmospheric drag [45]. In this approach, the radial distance r is the only spatial coordinate, so spherical symmetry is assumed. For that reason and since the atmospheric drag is the only considered perturbation, this formulation is only applicable after the band formation.

The vector field has then only one component

$$f_r = v_r n(r, t) \quad (8)$$

where v_r is the drift velocity in the radial direction.

According to the derivations in [40], under the hypothesis of quasi-circular orbits, v_r can be written as

$$v_r = -\varepsilon \sqrt{r} \exp\left(-\frac{r - R_h}{H}\right) \quad (9)$$

with $R_h = R_E + h_{ref}$, and the parameter ε collecting all the terms that do not depend on r

$$\varepsilon = \sqrt{\mu_E} c_d \frac{A}{M} \rho_{ref} \quad (10)$$

where μ_E is the Earth's gravitational constant; c_d is the drag coefficient of the fragment, assumed to be constant and equal to 2.2 [43]; A is the fragment cross-sectional area; and M is the fragment mass.

Though the method of the characteristics (Eq.7) can be written as a system of ordinary differential equations as [47]:

$$\begin{aligned} \frac{dr}{dt} &= v_r = -\varepsilon \sqrt{r} \exp\left(-\frac{r - R_h}{H}\right) \\ \frac{dn}{dt} &= -\left[\frac{2}{r} v_r + v_r'\right] n(r, t) \end{aligned} \quad (13)$$

6 FRAGMENTATION EFFECT ON THE BACKGROUND POPULATION

In this section the method introduced for the cloud propagation is applied to scenario E-5 (rocket stage impact at 1 km/s on ENVISAT centre of mass). For the purpose of studying the effect of a possible ENVISAT fragmentation, the evolution of the entire debris population is analysed, when at a certain instant ENVISAT collision takes place. The MASTER population for the IADC simulations is used as background debris population.

At the initial time, the spatial density function of the background population is computed, and it is propagated in time, following what was described in Section 5.3. Simultaneously, CSTS ENVISAT breakup model is used to characterise the fragments generated from the collision, in terms of characteristic length, area to mass ratio and velocity. The orbital elements of the produced fragments are propagated up to the band formation, when the continuum approach becomes applicable for the fragmentation cloud. At this time instant, the spatial density function of the fragmentation is built, and its contribution is added to the pre-existing debris population. Finally, the resulting spatial density function is propagated again, obtaining the evolution in time of the total debris population.

The evolution in time of the total debris population is shown in Fig. 13, from the band formation instant.

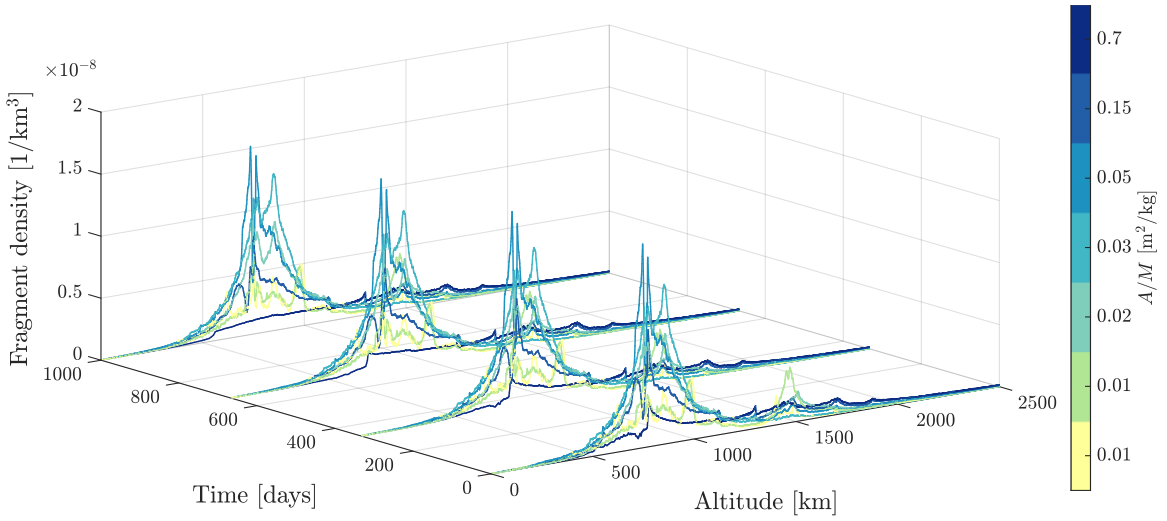

Figure 13: Evolution of the total spatial density function (time origin set at the band formation instant) for scenario E-5

In Fig 14, the spatial density function at the band formation is presented, for scenario E-5, before and after adding the fragmentation contribution. In this case, the band formation time is 721 days.

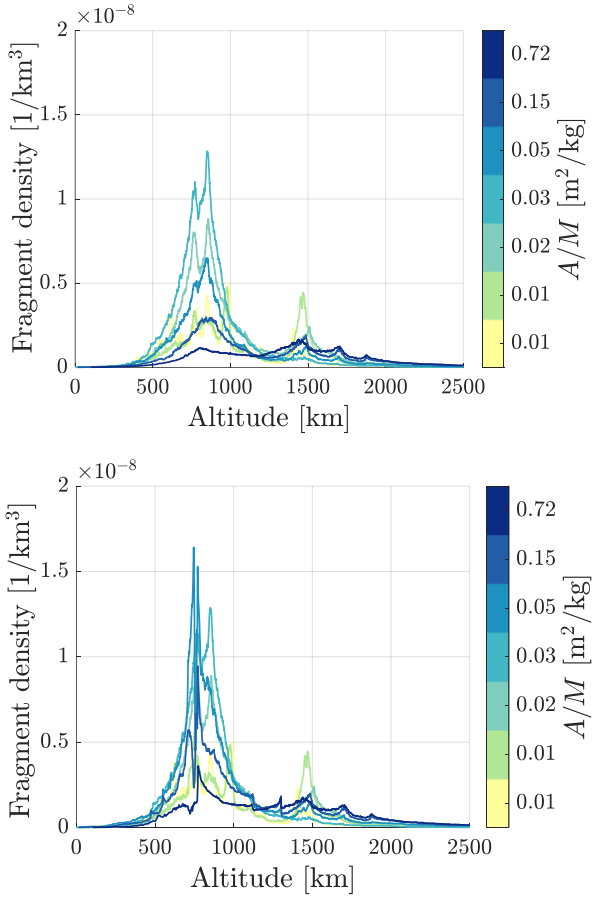

Figure 14: Spatial density function at the band formation, before (top) and after (bottom) adding the fragmentation contribution, for scenario E-5

The background population is divided into 7 A/m ratio bins, since the area to mass ratio is a key parameter determining not only the spatial/temporal evolution of the fragment due to atmospheric drag, but also the severity of a possible future impact [48]. The bins are defined so that each one contains the same number of objects at the initial time.

As can be noticed, ENVISAT fragmentation has a dramatic effect into the total space debris population, with an increase of the spatial density function higher than 400% at the altitude where the collision occurs.

7 CONCLUSIONS AND FUTURE WORKS

This paper presents a set of simulations performed with the Collision Simulation Tool Solver to investigate the collision of ENVISAT with a small satellite or a rocket stage. Characteristic length and area to mass distributions are generated for the simulated scenarios; results suggest that in general the NASA SBM overestimates the number of generated fragments. For a given EMR, it is shown that the geometry of the impact can influence not only the number of fragments but also the area to mass distributions; it can be observed that similar L_c distributions do not implicate comparable A/m ratio ones.

The fragments orbital propagation is performed for a single relevant scenario (rocket stage impact at 1 km/s on ENVISAT centre of mass). It is shown that a collision with ENVISAT can strongly increase the number of fragments currently in orbit, with an increase of the spatial density function higher than 400% at the altitude where the collision occurs.

Future works will focus on the scenarios whose simulations are still not complete; results will allow the identification of the most critical collision configurations and a more accurate assessment of the

appendages shielding effect. With the orbital propagation method introduced in this work the time evolution of the space debris environment will be evaluated for the other scenarios.

8 ACKNOWLEDGEMENTS

The research work presented in this paper is supported by the Italian Space Agency, in the framework of the ASI-INAF Agreement “Supporto alle attivita` lADC e validazione pre-operativa per SST (N. 2020-6-HH.0)”.

9 REFERENCES

[1] Kessler, D. J., & Cour-Palais, B. G. (1978). Collision frequency of artificial satellites: The creation of a debris belt. *Journal of Geophysical Research: Space Physics*, **83**(A6), 2637-2646.

[2] Alvarez, J., & Walls, B. (2016). Constellations, clusters, and communication technology: Expanding small satellite access to space. In *Aerospace Conference*, 2016 IEEE (pp. 1-11). IEEE.

[3] Karacalioglu, A. G., & Stupl, J. (2016). The Impact of New Trends in Satellite Launches on the Orbital Debris Environment. *NASA Technical Report. Houston, TX, United States* (2016)

[4] Foreman, V. L., Siddiqi, A., & De Weck, O. (2017). "Large satellite constellation orbital debris impacts: Case studies of oneweb and spacex proposals." *AIAA SPACE and Astronautics Forum and Exposition*. (p. 5200).

[5] Olivieri, L., & Francesconi, A. (2020). Large constellations assessment and optimization in LEO space debris environment. *Advances in Space Research*, **65**(1), 351-363.

[6] Klinkrad, H. (2017). Large satellite constellations and related challenges for space debris mitigation. *J. Space Saf. Eng*. **4**, 59–60.

[7] Lewis, H.G., Radtke, J., Rossi, A., Beck, J., Oswald, M., Anderson, P., Bastida Virgili, B., Krag, H. (2017). Sensitivity of the space debris environment to large constellations and small satellites. In: *Proc. 7th European Conference on Space Debris*, Darmstadt, Germany.

[8] Radtke, J., Kebschull, C., Stoll, E. (2017). Interactions of the space debris environment with mega constellations—using the example of the oneweb constellation. *Acta Astronaut.* **131**, 55–68.

[9] Rossi, A., Alessi, E.M., Valsecchi, G.B., Lewis, H., Radtke, J., Bombardelli, C., Virgili, B.B. (2017). A quantitative evaluation of the environmental impact of the mega constellations. In: *Proc. 7th European Conference on Space Debris*, Darmstadt, Germany.

[10] Virgili, B., Dolado, J., Lewis, H., Radtke, J., Krag, H., Revelin, B., Cazaux, C., Colombo, C., Crowther, R., Metz, M. (2016). Risk to space sustainability from large constellations of satellites. *Acta Astronaut.* **126**, 154–162.

[11] McKnight, D., Di Pentino, F., & Knowles, S. (2014). Massive Collisions In LEO - A Catalyst To Initiate ADR. In: *Proc. 65th International Astronautical Congress*, Toronto, CA.

[12] Secure World Foundation, 2009 Iridium-Cosmos Collision Fact Sheet, last updated Nov. 10, 2010. https://swfound.org/media/6575/swf_iridium_cosmos_collision_fact_sheet_updated_2012.pdf

[13] Letizia, F., Colombo, C., Lewis, H. G., & Krag, H. (2018). Development of a debris index. In *Stardust Final Conference* (pp. 191-206). Springer, Cham.

[14] Letizia, F., Colombo, C., Lewis, H., & Krag, H. (2017). Extending the ECOB space debris index with fragmentation risk estimation. In: *Proc. 7th European Conference on Space Debris*, Darmstadt, Germany.

[15] McKnight D., Speaks S., Macdonald J., Ebright K. (2018). Assessing Potential for Cross-Contaminating Breakup Events from LEO to MEO/GEO. In: *Proc. 69th International Astronautical Congress*, Bremen, Germany.

[16] Louet J., Bruzzi S. (1999) "ENVISAT mission and system." *IEEE 1999 International Geoscience and Remote Sensing Symposium. IGARSS'99 (Cat. No. 99CH36293)*, **3**, 1680-1682.

[17] ESA Envisat mission page: https://earth.esa.int/web/guest/missions/esa-operational-eo-missions/envisat (Available online Mar. 10, 2021)

[18] Lin, H. Y., & Zhao, C. Y. (2018). An estimation of Envisat’s rotational state accounting for the precession of its rotational axis caused by gravity-gradient torque. *Advances in Space Research*, **61**(1), 182-188.

[19] Sommer, S., et al. (2018). Temporal analysis of ENVISAT’s rotational motion. In *Proc. 7th European Conference on Space Debris*, Darmstadt, Germany.

[20] Flohrer, T., et al. (2015). Operational collision avoidance at ESOC. *Deutscher Luft-und Raumfahrtkongress, Rostok, Germany* 0270.

[21] Estable, S. (2016). Envisat removal by robotic capture means-results of the airbus ds led e. Deorbit Phase B1 ESA study. *ESA Clean Space Industrial Days, ESTEC, Netherlands*.

[22] Estable, S., et al. (2017) Definition of an Automated Vehicle with Autonomous Fail-Safe Reaction Behavior to Capture and Deorbit Envisat.

In *Proc. 7th European Conference on Space Debris*, Darmstadt, Germany.

[23] Hausmann, G., et al. (2015). "E. Deorbit mission: OHB debris removal concepts." *Proceeding of the 13th Symposium on Advanced Space Technologies in Robotics and Automation (ASTRA'2015),* Noordwijk, The Netherlands.

[24] Reynolds, R. C., et al. (1998). NASA standard breakup model 1998 revision. *Lockheed Martin Space Operations Report LMSMSS-32532, Houston, TX*.

[25] McKnight, D. S., Johnson, N. L., Fudge, M. L., & Maclay, T. D. (1995). Satellite orbital debris characterization impact test (SOCIT) series data collection report. *Kaman Sciences Corporation*.

[26] McKnight, D. S., Johnson, N. L., Fudge, M. L., & Maclay, T. D. (1995). Analysis of SOCIT debris data and correlation to NASA's breakup models. *Kaman Sciences Corporation*.

[27] Krisko, P. H., Horstman, M., & Fudge, M. L. (2008). SOCIT4 collisional-breakup test data analysis: With shape and materials characterization. *Advances in Space Research*, **41**(7), 1138-1146.

[28] Liou, J. C., Fitz-Coy, N., Clark, S., Werremeyer, M., Huynh, T., Sorge, M., ... & Opiela, J. (2013). DebriSat–A planned laboratory-based satellite impact experiment for breakup fragment characterization. In Proc. *Sixth European Conference on Space Debris.* Darmstadt, Germany

[29] McKnight, D., Maher, R., & Nagl, L. (1994). Fragmentation Algorithms for Strategic and Theater Targets (FASTT) Empirical Breakup Model, Ver 3.0. *DNA-TR-94-104, December*.

[30] McKnight, D., Maher, R., & Nagl, L. (1995). Refined algorithms for structural breakup due to hypervelocity impact. *International journal of impact engineering*, **17**(4-6), 547-558.

[31] Sorge M. E. (2008). Satellite fragmentation modelling with IMPACT. In: *Proc. AIAA/AAS Astrodynamics Specialist Conference and Exhibit*, Hawaii, USA.

[32] Sorge, M. E., & Mains, D. L. (2016). IMPACT fragmentation model developments. *Acta Astronautica*, **126**, 40-46.

[33] Francesconi, A., et al. (2019). CST: A new semi-empirical tool for simulating spacecraft collisions in orbit. *Acta Astronautica*, **160**, 195-205.

[34] Francesconi A., et al. (2019) Examination of satellite collision scenarios spanning low to hypervelocity encounters using semi-empirical models, In: *Proc. 70th International Astronautical Congress*, Washington, US.

[35] Sarego G. et al. (2019). Numerical evaluation of the influence of pre-arranged fault lines in the fragmentation of satellites subjected to hypervelocity collisions. *In: Proc. 70th International Astronautical Congress*, Washington, US.

[36] Colombo C., Letizia F., Lewis H. (2016). Spatial density approach for modelling of the space debris population, *26th AAS/AIAA Space Flight Mechanics Meeting*, Fe. 2016, AAS 16-465

[37] https://global.jaxa.jp/projects/sat/sds1/index.html (Available online Mar. 10, 2021)

[38] http://www.braeunig.us/space/specs/lgmarch.htm (Available online Mar. 10, 2021)

[39] Le May, S., et al. (2018). Space debris collision probability analysis for proposed global broadband constellations." *Acta Astronautica*, **151**, 445-455.

[40] Letizia, F., Colombo, C. & Lewis, H.G. (2015). Analytical Model for the Propagation of Small-Debris-Object Clouds After Fragmentations. *Journal of Guidance, Control, and Dynamics*, **38**(8), 1478-1491.

[41] Jehn, R. (1991). Dispersion of Debris Clouds from In-Orbit Fragmentation Events. *ESA Journal*, **15**(1), 63-77.

[42] Ashenberg, J. (1994). Formulas for the Phase Characteristics in the Problem of Low-Earth-Orbital Debris. *Journal of Spacecraft and Rockets*, **31**(6), 1044-1049.

[43] Vallado, D. A. (2013). *Fundamentals of Astrodynamics and Applications, 4th ed.*, Springer, New York, NY, pp. 628–637.

[44] King-Hele, D. (1987). *Satellite Orbits in an Atmosphere: Theory and Application*, Blackie, Glasgow, pp. 44–62.

[45] Kessler, D.J. (1981). Derivation of the Collision Probability between Orbiting Objects: The Lifetimes of Jupiter's Outer Moons. *Icarus*, **48**(1), 39–48.

[46] McInnes, C. R. (2000). Simple Analytic Model of the Long Term Evolution of Nanosatellite Constellations. *Journal of Guidance, Control, and Dynamics*, **23**(2), 332–338.

[47] Letizia, F. (2015). *Space Debris Cloud Evolution in Low Earth Orbit*. PhD thesis. University of Southampton.

[48] McKnight, D. S. (1991). Determination of Breakup Initial Conditions. *Journal of Spacecraft and Rockets*, **28**(4), 470–477.